RESEARCH ARTICLE

ADVANCED FUNCTIONAL MATERIALS
www.afm-journal.de

Continuous Nanoparticle Patterning Strategy in Layer-Structured Nanocomposite Fibers

*Weiheng Xu, Rahul Franklin, Dharneedar Ravichandran, Mohammed Bawareth, Sayli Jambhulkar, Yuxiang Zhu, Mounika Kakarla, Faizan Ejaz, Beomjin Kwon, Mohammad K. Hassan, Maryam Al-Ejji, Amir Asadi, Nikhilesh Chawla, and Kenan Song**

Anisotropic polymer/nanoparticle composites display unique mechanical, thermal, electrical, and optical properties depending on confirmation and configuration control of the composing elements. Processes, such as vapor deposition, ice-templating, nanoparticle self-assembly, additive manufacturing, or layer-by-layer casting, are explored to design and control nanoparticle microstructures with desired anisotropy or isotropy. However, limited attempts are made toward nanoparticle patterning during continuous fiber spinning due to the thin-diameter cross section and 1D features. Thus, this research focuses on a new patterning technique to form ordered nanoparticle assembly in layered composite fibers. As a result, distinct layers can be retained with innovative tool design, unique material combinations, and precise rheology control during fiber spinning. The layer multiplying-enabled nanoparticle patterning is demonstrated in a few material systems, including polyvinyl alcohol (PVA)–boron nitride (BN)/PVA, polyacrylonitrile (PAN)–aluminum (Al)/PAN, and PVA–BN/graphene nanoplatelet (GNP)/PVA systems. This approach demonstrates an unprecedentedly reported fiber manufacturing platform for well-managed layer dimensions and nanoparticle manipulations with directional thermal and electrical properties that can be utilized in broad applications, including structural supports, heat exchangers, electrical conductors, sensors, actuators, and soft robotics.

1. Introduction

Polymer composites have been extensively studied over the past decades for their lightweight, low cost, processability, and tunable functional properties.[1] Homogeneous mixing between nanoparticle fillers and polymer matrices for synergistic and hybrid properties has been the most adopted strategy for fabricating composites with isotropic properties.[2] On the other hand, new processes have been developed to achieve a higher degree of freedom in particle morphology and conformation control, such as ice-templating,[3,4] layer-by-layer casting,[5,6] additive manufacturing,[7–10] field-assisted nanoparticle patterning,[11,12] and particle self-assembly.[13,14] These procedures generate ordered particle microstructures with tailored packing factors or orientations for anisotropic properties.[15] For example, ice-templating can create a myriad of microstructures and microarchitectures, where particle fillers are arranged in lamellar, radially aligned, or honeycomb structures. These composites are usually coupled with property anisotropy, e.g., unidirectional ionic conductivity in composite electrolytes or cell alignment in tissue scaffolds.[16,17]

Beyond comfort or aesthetic, polymer composite-based functional textiles have recently gained much attention as wearable sensors,[18–21] energy devices,[22–24] and intelligent products.[25–28] There have been efforts and progresses made toward

---

W. Xu, D. Ravichandran, M. Bawareth, S. Jambhulkar, Y. Zhu
The Polytechnic School (TPS)
Ira A. Fulton Schools of Engineering
Arizona State University
Mesa, AZ 85281, USA

R. Franklin, N. Chawla
School of Materials Engineering
Purdue University
West Lafayette, IN 47907, USA

M. Kakarla, F. Ejaz, B. Kwon
School for Engineering of Matter
Transport and Energy (SEMTE)
Arizona State University
Tempe, AZ 85287, USA

M. K. Hassan, M. Al-Ejji, K. Song
Center for Advanced Materials
Qatar University
P.O. Box 2713, Doha, Qatar

A. Asadi
Department of Engineering Technology and Industrial Distribution
Department of Materials Science and Engineering
Texas A&M University
College Station, TX 77843-3367, USA

K. Song
The School of Manufacturing Systems and Networks (MSN)
Ira A. Fulton Schools of Engineering, Arizona State University
Mesa, AZ 85212, USA
E-mail: kenan.song@asu.edu

The ORCID identification number(s) for the author(s) of this article can be found under https://doi.org/10.1002/adfm.202204731.

DOI: 10.1002/adfm.202204731

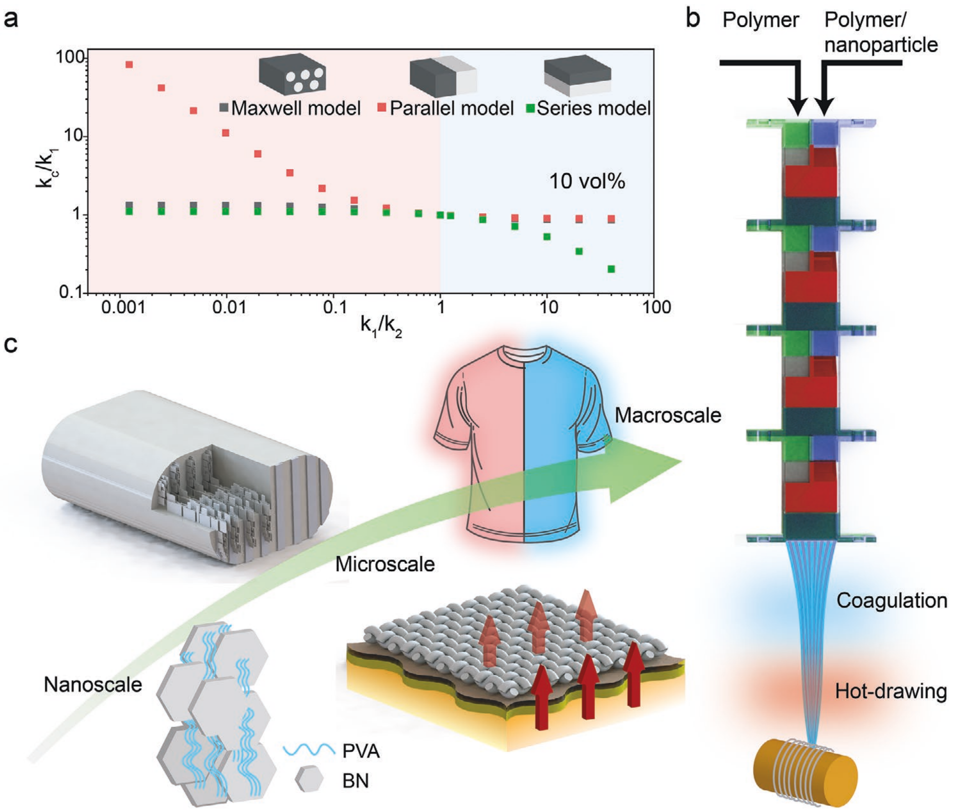

Figure 1. a) Comparisons among the Maxwell–Eucken, Parallel, and Series models (inset illustrations) for predicting the thermal conductivity of composites (k_c) as a function of different thermal conductivity ratios between the polymer (k_1) and nanoparticle (k_2) phases.[37] Nanoparticle loading is maintained at 10 vol%. b) A schematic illustration of in-house-developed multilayering technique as a unique spinning for multiphase and multimaterial fibers. c) Schematic illustrations of the hierarchically structured composites, from nanoscale layers to microscale fibers to macroscale fabrics, with thermoregulation application for demonstration.

functionality-driven systems, such as stretchability,[29,30] self-healing,[31] self-powering,[32,33] shape memory,[34] biodegradabilities,[32,35] and biocompatibility[36] in wearable devices. Among many functions that smart textiles can offer, passive thermoregulating can manipulate heat generation or dissipation without external energy input, thus benefiting cost efficiency and sustainability.[25] Many theoretical models have suggested that thermal conductivity is heavily dependent on the microstructure of nanoparticles and polymer matrices.[37–39] For example, **Figure 1**a shows the thermal conductivity differences among Maxwell–Eucken, Series, and Parallel models, where k_1, k_2, and k_c represent the thermal conductivity parameters for polymer, nanoparticle, and composite materials, respectively. For thermal-insulating composite, $k_1/k_2 > 1$, the Series model shows a much lower k_c, whereas for thermal-conductive composite, $k_1/k_2 < 1$, the Parallel model shows a much higher k_c.[40,41] Previous studies on passive thermoregulation composite fibers primarily reflect the Maxwell–Eucken model since complex microstructure control in textile fibers remains a challenge due to the microscale fiber dimension and production continuation requirements.[42–45] Structures, such as core–shell,[46–48] islands-in-the-sea,[49] side-by-side,[50] and segmented fibers,[51,52] are some of the most researched examples. Nevertheless, their dimensional feature size directly correlates to the spinneret geometry limited by tooling resolution and precision engineering. For example, our group previously reported a trilayered, coaxial fiber with two polymer channels sandwiching a conductive middle channel for simultaneously achieving electrical conductivity, volatile sensitivity, and high stretchability.[53] Nevertheless, the lack of spinning apparatus control (e.g., oversized spinneret exit, irregular internal dimensions, or unexpected wall roughness) resulted in inefficient interface or phase interactions and, thus, suboptimal performance that is not suitable for advanced applications.

To overcome similar issues, we combined a layering technique with dry jet–wet fiber spinning to generate multilayered composite fibers, where nanoparticles were selectively deposited at desirable locations with patterning resolutions enhanced by tooling engineering.[54] Through our unique flow behavior-driven layer-multiplying process (Figure 1b), the layer domain size was controlled on the nanometer scale (depending on nanoparticle dimensions and geometry) while the spinneret size was maintained at the macroscale.[55–58] For the first time, this research demonstrates the potential of fabricating anisotropic fibers with highly hierarchical laminating structures. Nanoscale boron nitride (BN) (Figure 1c), based on covalently bonded boron and nitride layers known for their high thermal conductivity,[59] is selected as the first example to examine layer manufacturability and heat dissipation capabilities (Figure 1c). As a result of the nanoparticle assembly and alignment, conductive pathways are formed along continuous BN channels within polymeric fibers that were flexibly woven as textiles for passive thermoregulation control on the macroscale (Figure 1c). Furthermore, the obtained nanoparticle patterns display an ordered lamella structure consistent with the Parallel model, with mechanical and thermal properties investigated experimentally and validated computationally. The demonstrations of two other polymer/particle combinations also suggest broad applications of our facile and effective fiber spinning strategy in porous media and high-performance composite/hybrid systems.

2. Results and Discussion

Manipulating continuous fiber microstructures and hierarchies have been challenging due to the small-sized diameter, thus, requiring a delicate design of manufacturing processes to precisely control the fiber spinning dynamics. The layer multiplying technique (Figure 1b), as a new tooling engineering for fiber and textile engineering, has not been reported in the literature except for ours.[54,60] The multimaterial layering mechanism mimicking laminate structures is described in Figure S1 (Supporting Information). As two precursor feedstocks entered one multiplier, they were split horizontally and rearranged vertically, transforming two adjacent layers into four alternating layers. Each time an additional multiplier was added, the layer number doubled while the layer thickness was halved. Consequently, a number of n multipliers produced 2^{n+1} layers. The utilization of 3D printing could rapidly prototype parts (e.g., spinneret and multipliers) with proper dimensions and internal complexities, enabling fibers with varying microstructures (e.g., flexibility with core–shell, hollow, pie, and layered morphologies (Figure 1c)), flexible material combinations (**Table 1**), and layer resolutions (e.g., an inlet size of 1 mm leads to a layer domain size of ≈488 nm after going through ten multipliers).

The rheological properties play a vital role in retaining formed layers of desirable dimensions and compositions during the layer multiplying procedures. For example, different polyvinyl alcohol (PVA) and BN combinations were studied for optimized rheology (Figure S2, Supporting Information) and stable colloidal states (Figure S3, Supporting Information). BN nanoparticle used in this work has an average lateral dimension of 340 nm ± 140 nm according to scanning electron microscope (SEM) analysis (Figure S4, Supporting Information). The measured viscosities (Pa s) at a shear rate of 1 s^{-1} and the damping parameter ($\tan(\delta)$) values are shown in **Figure 2**a,b, with indicated green regions corresponding to the spinnability window because of the fiber gelation capability and solidification kinetics. First, uniform layers need to be formed via a low Reynolds number (Re) where the inertia is negligible compared to viscous and pressure forces (e.g., Re = 0.05 to form sheet-like liquid flows).[61] By fixing the characteristic linear dimension (L, m) and fluid density (ρ, kg m^{-3}), a minimally required liquid viscosity of 5 Pa s was calculated based on the equation of $\mathrm{Re} = \rho v L\ \eta^{-1}$, where v is the flow speed (m s^{-1}) (Figure 2c). Besides, a maximum viscosity was limited to 100 Pa s for material working with our syringe pump, thus satisfying the layer formation requirement.

Second, the polymer chains must form strong enough entanglement within each constrained and size constantly changing channels during layer multiplying to avoid interlayer diffusions. As a simple demonstration, Figure 2d shows the fiber pulling effects of 20 wt% PVA and 5 wt% PVA/50 vol% BN solutions, both with a zero shear viscosity higher than 10 Pa s followed by a viscosity plateau (Figure S2, Supporting Information), favoring fiber gelation and layer retention in separate channels during fiber spinning.[62] PVA's high viscosity also prevented the transport of the adjacent BN nanoparticles across the layer interfaces, with a stable solution/suspension interface, shown in Figure S5 (Supporting Information). For comparison, lower PVA viscosity failed to prohibit interlayer nanoparticle diffusions and resulted in uneven BN distributions (i.e., layer disruptions in Figure S3a,b vs retaining layers in Figure S3c in the Supporting Information).

Third, as a feature of viscoelasticity, shear-thinning behavior is essential to colloidal dope spinnability.[63] As rigid BN nanoparticles can be assumed to be perfectly elastic,[64] their increased concentration in viscous PVA solutions would penetrate between the polymer chains and lower their networking/entanglement, reducing their flowability, especially within a shear field that may cause nanoparticle alignment.[65] At a

Table 1. Summary of the spinning dope compositions and fiber terminologies (Note: For fibers with uniform structure, layers A and B have the same composition. For example, U0% represents uniform structured fibers with 0 vol% BN. For fibers with multilayer structure, layer A is pure PVA and layer B is BN/PVA, and x represents the number of layers. For example, 32L10% represents 32 alternating layers with 10 vol% BN. All wt% are weight percentages of the polymers with respect to the solvent, and vol% are volume percentages of BN with respect to the polymer content).

Structure	Overall BN concentrations [vol%]	Layer A composition	Layer B composition	Terminology
Uniform	0	20 wt% PVA		U0%
	5	5 vol% BN, 18 wt% PVA		U5%
	10	10 vol% BN, 15 wt% PVA		U10%
	20	20 vol% BN, 10 wt% PVA		U20%
	30	30 vol% BN, 10 wt% PVA		U30%
	40	40 vol% BN, 8 wt% PVA		U40%
Multilayer	5	20 wt% PVA	10 vol% BN, 15 wt% PVA	*x*L5%
	10	18 wt% PVA	20 vol% BN, 10 wt% PVA	*x*L10%
	20	15 wt% PVA	40 vol% BN, 8 wt% PVA	*x*L20%

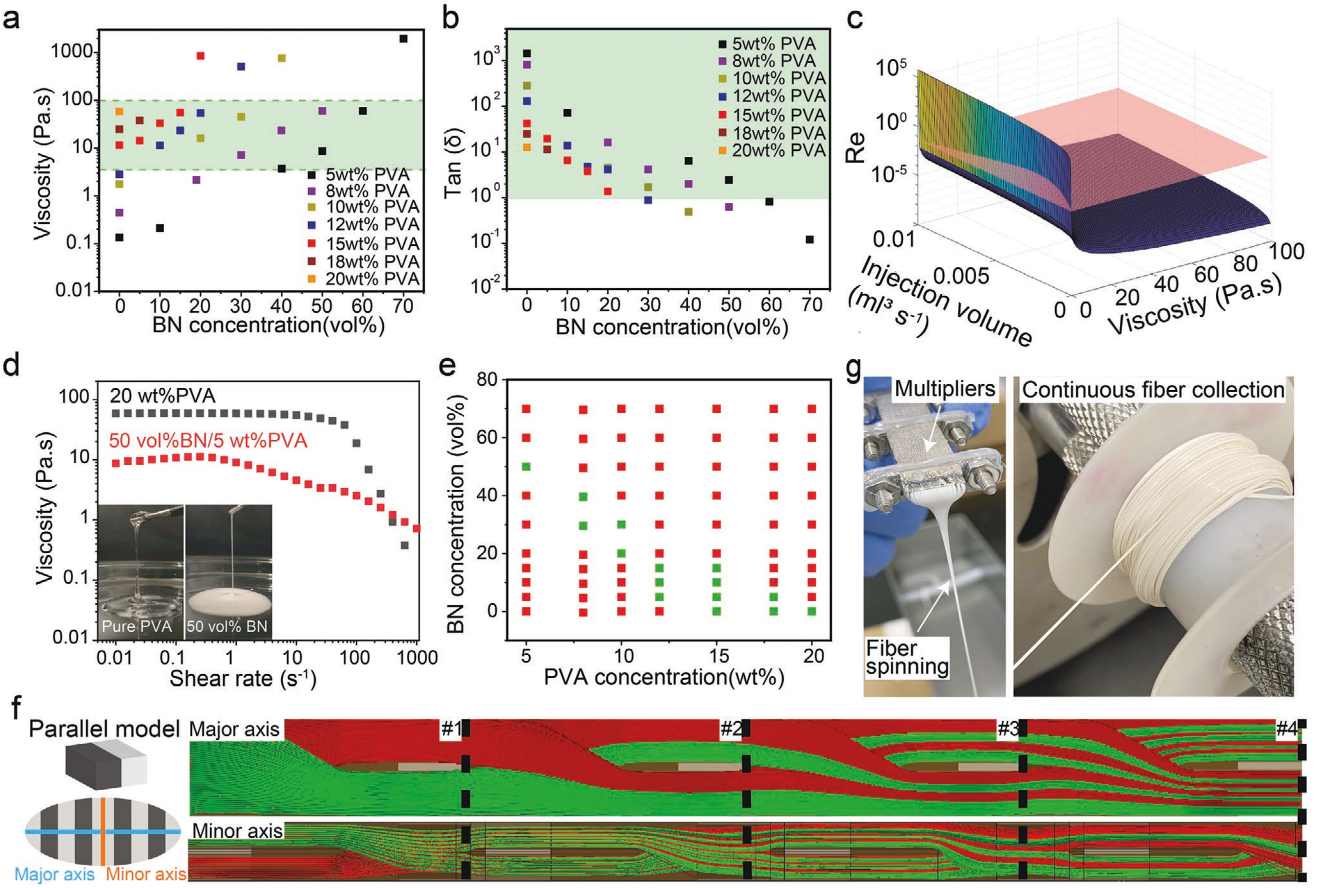

Figure 2. Material composition optimizations for fiber spinnability and property enhancement purposes. a) Viscosity at a shear rate of 1 s^{-1} and b) tan(δ) at different BN and PVA concentrations. c) The theoretical calculation of Re as a function of injection volume and viscosity during the liquid flow extrusion. d) The viscosity of pure PVA solution and BN/PVA suspensions, with insets showing the fiber-pulling effect of pure PVA and 50 vol% BN/PVA solutions. e) The fiber composition spinnable window where the green regime indicates successful and red indicate failure. f) CFD simulations of the layer formability of the 16L10% fiber going through four multipliers (#1–4). Green and red regimes indicate the PVA/DMSO solution and the PVA/BN/DMSO suspension, respectively. g) Photographs of the fiber spinning setup and the continuous fiber collection process.

certain point, the excessive BN would change the solution's flow behavior from pseudoplastic (i.e., shear thinning) to dilatant (i.e., shear thickening) (Figure S2, Supporting Information), unfavorable for shearing-involved extrusion and injections.[65] As a result, the gelation point where tan(δ) equals 1 was used as one of the criteria for the least-satisfying flow behavior (Figure 2b). By varying the polymer or nanoparticle concentrations of each spinning dope system, a phase diagram of the PVA/BN system is shown in Figure 2e, with the green dots illustrating the spinnable window; the highest achievable BN concentration was determined at 50 vol% within the 5 wt% PVA/dimethyl sulfoxide (DMSO) solutions.

Last but not least, the viscosity matching between alternating layers is critical to achieving intact and distinct layering (Figure S6a, Supporting Information). As a comparison, optical images suggest a high-viscosity mismatch would result in nonuniform layer thicknesses and layering disruptions (Figure S6b, Supporting Information) with the same spinning parameters (e.g., injection/collection rates and coagulation environment). The computational fluidic dynamic (CFD) simulation was used to visualize the layer multiplying efficiency with different viscosity combinations (Figure S6c–e, Supporting Information). The gradual increase in the layer thickness mismatch with respect to layer viscosity differences indicates that layer disruption is a gradual process, which aggravates with increased viscosity mismatch (Figure S6f–h, Supporting Information). Figure 2f shows the CFD simulation of a 16L of 10% fiber with dissections shown in Figure S7 (Supporting Information). Uniform layers were successfully formed by matching the viscosity between 18 wt% PVA and 20 vol% BN in 10 wt% PVA (i.e., 60 and 58 Pa s, respectively, at a shear rate of 1 s^{-1} (Figure 2a)). By using four multipliers, two adjacent PVA and BN/PVA layers were multiplied into 16 layers across the major axis, and the composition remained the same across the minor axis. Figure 2g shows the fiber spinning and the continuous fiber collection processes. Table 1 summarizes the compositions and terminology of various fiber types, with the rest of the samples studied in the following sections.

Differential scanning calorimetry (DSC) results show that the glass transition temperature (T_g) consistently increases with higher BN concentrations (**Figure 3**a). Peak T_g occurs at 30 vol% BN at 75.8 °C, about 16 °C higher than the pure PVA. Due to their constraining effect at the polymer/nanoparticles interface, the addition of BN nanoparticles increased

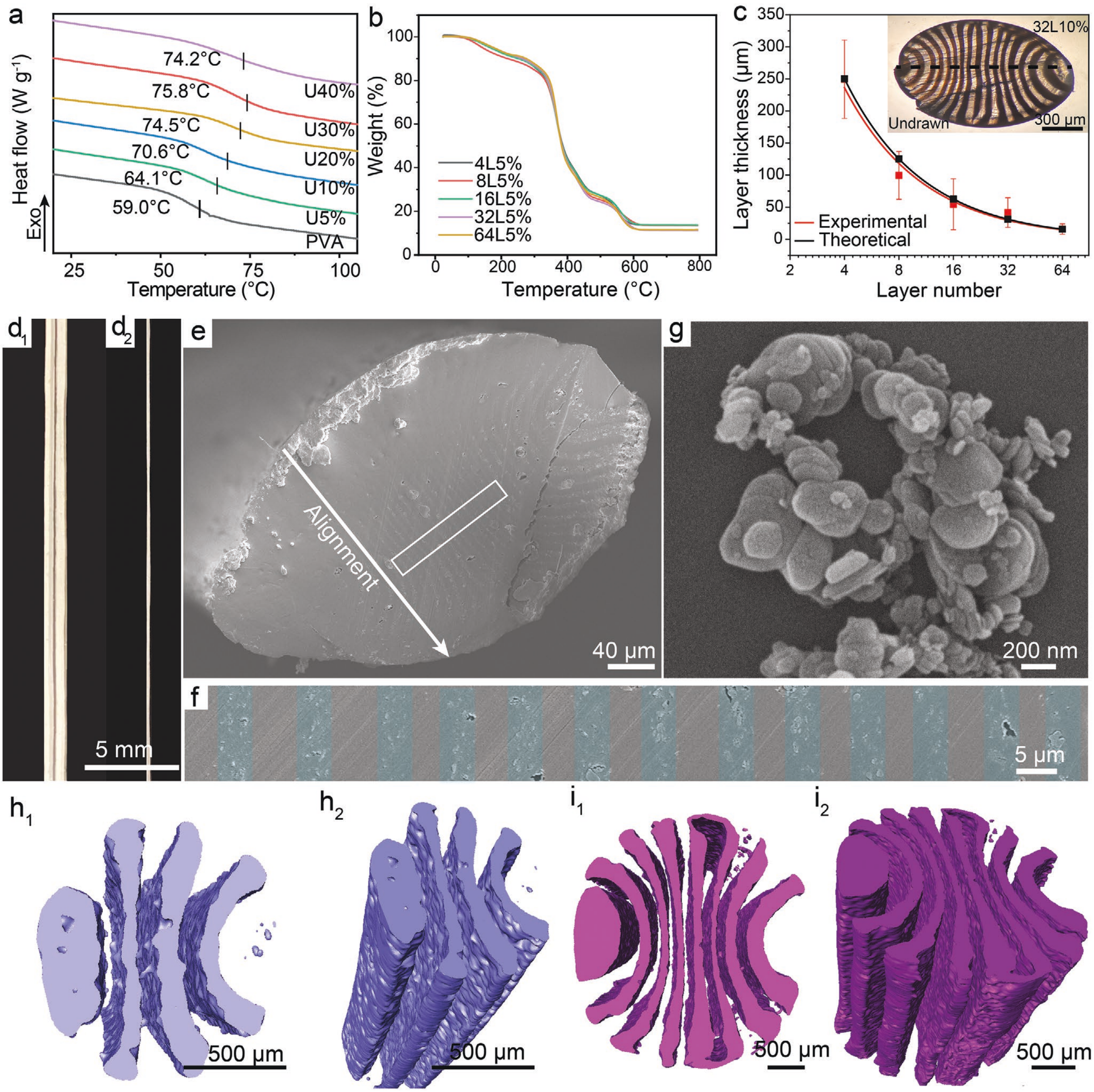

Figure 3. a) DSC results of uniform composite fibers show the thermal resistance enhancement with higher BN/PVA volume percentages (vol%). b) TGA results of 5 vol% BN/PVA fibers with different layer numbers show constant BN volume percentage. c) Experimentally measured and theoretically predicted layer thickness along the dotted black line with increased layer numbers. SD is shown for measured values. d_1,d_2) Optical images of the as-spun 64L10% fiber from the major and minor axes, respectively. Cross-sectional SEM images of e) the postdrawn 64L10% fiber with zoom-in regions showing the f) BN layers with falsified coloring and g) BN nanoparticle morphology. Micro-CT images of the 3D continuous BN channels for h_1,h_2) 8L10% and i_1,i_2) the 16L10% fibers from the h_1,i_1) top and h_2,i_2) oblique views.

the rigidity of the PVA polymer chains and the resistance to thermal transitions (e.g., T_g). At 40 vol%, a slight decrease in the T_g suggests a less efficient constraining effect, which could be caused by the increase of the BN–BN interface due to particle agglomeration. Since BN shows no weight degradation under an air atmosphere and PVA degrades 100% up to a temperature of 800 °C, the thermogravimetric analysis (TGA) is an accurate way of determining the fiber compositions. Figure 3b shows the degradation curves of 5 vol% (i.e., ≈10 wt%) fibers with layer numbers ranging from 4 to 64. Their weight residues have an average of ≈10 wt% and a standard deviation (SD) of ±1.1%, showing high composition consistency during the layer multiplication process. There are mainly three degradation sections, i.e., evaporation of water/solvent residue before

200 °C, decomposition of PVA side chains starting at 300 °C, and decomposition of PVA main chains starting at 550 °C.[66] Figure S8a (Supporting Information) shows the TGA curves of BN powder, pure PVA, 32 L5%, 32 L10%, and 32 L20% fibers, and Figure S8b (Supporting Information) shows the slight differences between measured weight residue with theoretically predicted values, indicating precise layer composition control and structural consistency.

The thickness of the BN layer was reduced to half with each multiplier addition during fiber spinning. Figure 3c shows the experimentally measured and theoretically calculated layer thicknesses across the middle dotted line for the 4–64 layered undrawn fibers. The SD gradually improves with increased layer numbers. After fiber drawing, the layer thickness decreased further, reaching to as small as 2 µm for the 128L10% fibers (Figure S9, Supporting Information). After spinning, the designed rectangular nozzle enables an elliptical fiber shape with major and minor axes due to the drawing effects (Figure 3d). The cross-sectional SEM images of the 64L10% fiber confirm such a morphology after the hot drawing (Figure 3e). The size aspect ratio of the ellipse is ≈1.5, where the lengths of the major and minor axes are 350 and 235 µm, respectively. This aspect ratio can be controlled by the nozzle shape design readily accessible via our 3D-printed spinning setup; photographs of exiting nozzles with aspect ratios of 1, 2, and 10, and their corresponding fiber cross-sectional SEM images with aspect ratios of 1, 1.5, and 2.5 are shown in Figure S10 (Supporting Information). For the 64L10% fiber, BN layers follow a periodic pattern across the major axis, with individual layers aligning along the minor axis (Figure 3e). Each layer's thickness approximately equals 4 µm, as shown in the colored regimes in Figure 3f. Within each layer, BN nanoparticles of sizes varying from 300 nm to 1 µm are interconnected to form thermally conductive pathways (Figure 3g). To further examine the fiber morphology and their channel continuity, micro-X-ray microtomography (micro-CT) was used for the undrawn 8L10% (Figure 3h_1,h_2) and 16L10% (Figure 3i_1,i_2) fibers. Note that layer thickness smaller than 20 µm could not be observed via micro-CT due to voxel resolution and contrast limit. The continuous BN channels are highlighted in blue and purple, while the pure PVA channels are transparent (Figure 3h,i). The continuous channels indicate layer continuity and composition consistency along the fiber axial direction, consistent with the TGA characterizations (Figure 3b). However, the channels are not perfectly aligned in the direction across the fiber. Figure S11a (Supporting Information) shows the layer thickness distribution across the fiber; layers in the middle tend to be more uniform compared to layers on the edges. We believe that this curling of the layers could affect the fiber performance and is caused by the solvent exchange process during the coagulation of the fiber. Before the polymer gels exit the nozzle, the PVA and BN/PVA layers display well-defined layer-by-layer vertical patterns (Figure S11b, Supporting Information). As they exit the nozzle and enter the coagulation bath, the concentration-gradient-driven solvent exchange process between the solvent (DMSO) and nonsolvent (methanol) reshapes the fiber morphology from rectangular to elliptical (Figure S11c,d, Supporting Information). During this process, the higher solvent concentration gradient at the fiber edge results in more layer curling and the lower solvent concentration gradient at the fiber middle section results in less layer curling.

After establishing the alternating layered structure, fibers were drawn above their T_g to align the polymer chains, reduce the fiber diameter (i.e., better size effects due to lower defect density), and increase structural properties.[67] During the fiber drawing process, the polymer chains reoriented themselves along with the fiber axial direction and increased their chain density, promoting better uniaxial mechanical properties (e.g., better anisotropic modulus and strength at 180 than 25 and 100 °C drawing, respectively).[68] Stress–strain curves for the postdrawn uniform fibers are shown in **Figure 4**a. The addition of BN, even at a 5% concentration, results in inferior ultimate tensile strength performances; at a 40% loading, the tensile strength is reduced by about 77% (i.e., PVA vs U5–40% composites; Figure S12a, Supporting Information). Note that the BN inclusion in this research (e.g., volume percentage = 5–40%) is higher than most literature reports,[69] and we do not expect higher mechanical properties as BN–BN interfaces do not transfer stress efficiently according to composite mechanics.[70] Similarly, fracture strain values also decrease with increased BN particle loading (Figure 4a). Micro-CT scan imaging shows trails of voids along the fiber axial direction after the drawing process (Figure S13, Supporting Information), which are likely the leading causes of lowered tensile strength (Figure S12a, Supporting Information). Their formations are resulted from the polymer chain movement when the shear stress generated during the fiber drawing process could not overcome the momentum needed to exfoliate/redistribute the large BN clusters. Another cause could be the higher T_g of BN-containing fibers as their polymer chain mobilities are more resistant to drawing temperatures. Therefore, an additional drawing step at 180 °C was used (Figure S12b, Supporting Information). As a result, for pure PVA fibers, the percentage increase in strength from 100 to 180 °C is almost negligible; however, for the U10%, U20%, and U30% fibers, the increments are 19.7%, 54.7%, and 80.5%, respectively (Figure S12b, Supporting Information). Although the performance gaps between the BN-containing and pure PVA fibers become narrower at higher drawing stages, additional loading of BN nanoparticles still deteriorates fiber strength. Young's modulus is less affected by the addition of BN; a 10% increase is observed for the U5% fiber, and a 25% decrease is observed for the U30% fiber (Figure S12c,d, Supporting Information). A noticeable 64% decrease is observed as BN volume concentration increased to 40%, which was expected as previous DSC data suggested the higher BN/BN interfaces, resulting in lower load transfer efficiency.[71]

Through the multilayering process, selective spatial deposition of the BN nanoparticles was controlled as they occupy half of the fiber volume. At equal BN loadings of 10 and 20 vol%, layered composites show lower Young's modulus and ultimate tensile strength than uniformly structured fiber (U-type fibers, Figure 4b), consistent with the rule of mixture calculations.[72,73] The relationship between layer numbers and mechanical properties was further investigated; the 32L10% fiber peaks the performances in both modulus and strength by 68% and 5% increases compared to the 4L10% fiber, respectively (Figure 4c). Also, a finite element modeling (FEM) simulation was conducted on a composite consisting of alternating layers with

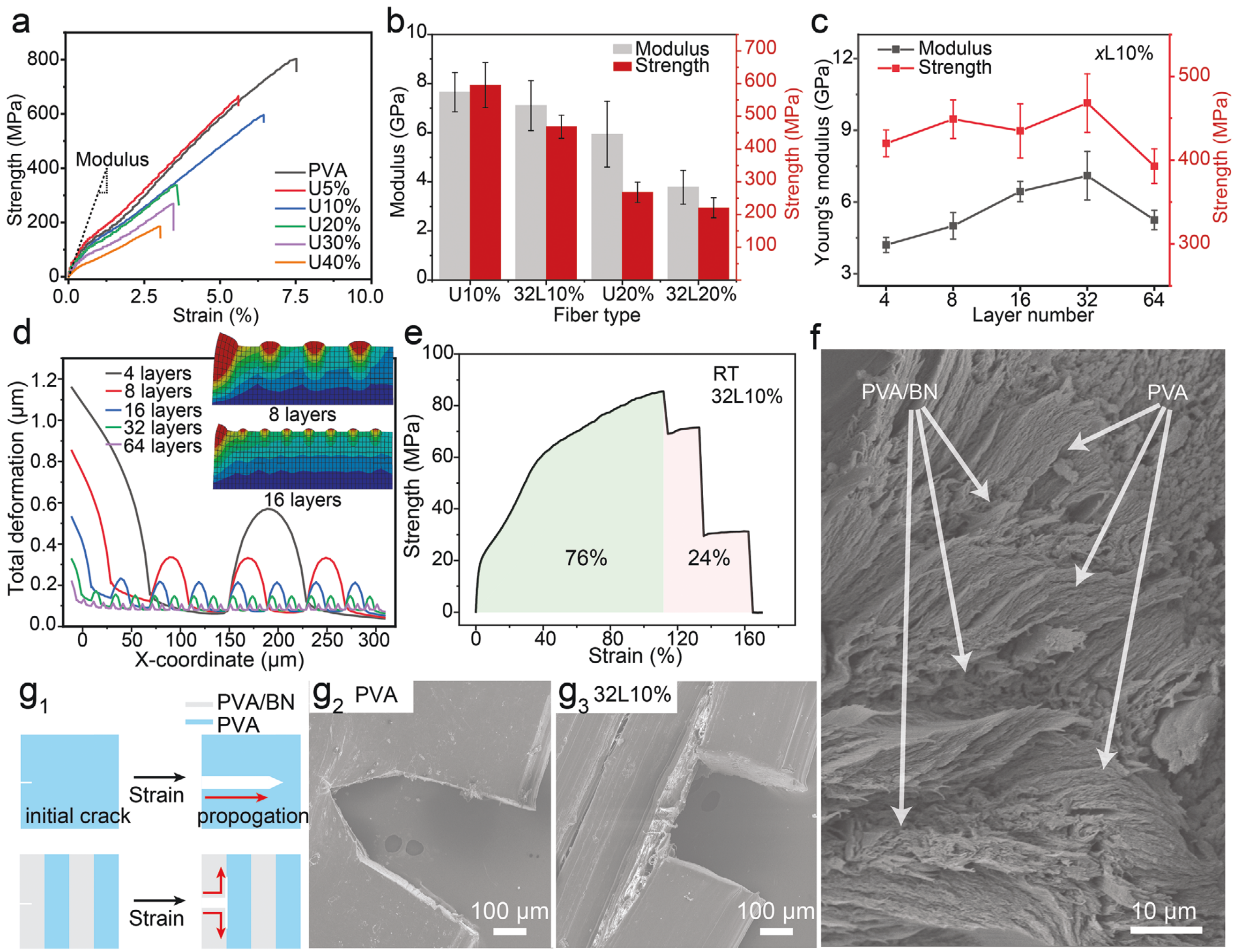

Figure 4. Mechanical properties of uniform and layered fibers as a function of the fiber compositions and layering numbers. a) Stress–strain curves of uniform fibers with different BN loadings after hot drawing at 100 °C. b) Comparisons of Young's modulus and ultimate tensile strength between the uniform and 32-layered fibers after hot drawing at 100 °C. c) Relationships of Young's modulus and ultimate tensile strength values with different layer numbers. SDs are shown for panels (b) and (c). d) Deformation simulations of fibers with different layer numbers via FEM. e) The stress–strain curve of 32L10% fibers drawn at room temperature showed a stepwise fracture. f) SEM images of the 32L10% fibers showed distinct surface morphologies within the PVA and PVA/BN layers during fracture. g_1) Schematics showing the crack propagation route with g_{2},g_{3}) the SEM images of propagated cracks in PVA and 32L10% fibers, suggesting that the BN-containing layers served as crack barriers or reflectors.

different stiffnesses, fixed bottom layers, and uniformly distributed force on the top surface (insets in Figure 4d). Since both layers consisted of PVA as the polymer matrix, their interface was assumed to be perfectly bonded at the initial deformation. The simulation results show that the total deformation on the surface reduces with reduced layer thicknesses (Figure 4d; Figure S14a,b, Supporting Information), inferring an increased interfacial interaction would increase the composite stiffness. Similar mechanical behaviors have been observed in previous composite laminates with varying thicknesses of metal alloys.[74]

Moreover, the stress–strain profiles for the 32L10% fibers show stepwise fracture behavior (Figure 4e; Figure S14c, Supporting Information) for fibers drawn at room temperature and 100 °C, respectively), which is different from U10% fibers, where a linear elastic response is observed until a catastrophic failure (Figure 4a). SEM images show two distinct types of fractures, with the BN/PVA layer failing in a brittle fashion showing a clean-cut cross section, while the PVA layer fails in a ductile fashion with a fiber bridging phenomenon (Figure 4f; Figure S15, Supporting Information). Based on this observation, it can be concluded that the BN/PVA layers are subjected to the mechanical tension within the elastic regions at first, followed by an extension of the PVA layer in a plastic zone until the complete fracture. This alternating layered structure could be one of the ways to increase the pseudoductility of high-modulus fibers. Moreover, the alternating layered structure also shows crack deflection behavior. An initial crack was introduced manually to both pure PVA and 32L10% fibers, and upon 4% strain, two fibers show noticeable differences (Figure 4g_1–g_3). Unlike PVA fiber, 32L10% fiber inhibits crack propagation by deflecting its direction in the axial direction rather than across the fiber. It is worth mentioning that, for the 32L10% fiber drawn at room temperature, ≈24% of the total energy absorbed is succeeding from the beginning of the stepwise fracture (Figure 4e). This enhanced fracture resistance is likely due to the different mechanical properties between the layers, resembling the previously reported interlayer technique in laminates for toughness improvement.[73] Tables S2–S5 (Supporting Information) show the mechanical properties and energy absorptions for the 4L10%, 32L10%, 64L10%, and 128L10% fibers. Interestingly, as layer number increases, the percentage of fibers under tensile test showing stepwise fracture characteristic decreases, 100% for 4L10%, 60% for 32L10%, 20% for 64L10%, and 0% for 128L10% (Figure S14d, Supporting Information). This implies that with increased layer numbers, the fiber gradually transformed from a multilayered composite to a more uniformly phased composite.

The unique layers can facilitate directional heat dissipation or conduction. By assuming that the BN/PVA composite phase follows the Maxwell–Eucken model, a Parallel–Maxwell–Eucken model for the thermal conductive composite was proposed according to Equations (1) and (2) (Figure S16a, Supporting Information) because of the parallel combinations of layers, where k_p, k_m, k_n, and k_2 are the thermal conductivities of the composite layers, polymer matrix, nanoparticle, and polymer/nanoparticle phase, v_n is the volume fraction of the nanoparticles, and v_2 is the volume fractions of polymer/nanoparticle phase which was assumed to be 0.5[37]

$$k_\mathrm{p} = k_\mathrm{m}\left(1 - v_2\right) + k_2 v_2 \tag{1}$$

$$k_2 = k_\mathrm{m} \frac{2k_\mathrm{m} + k_\mathrm{n} - 2\left(k_\mathrm{m} - k_\mathrm{n}\right) v_\mathrm{n}}{2k_\mathrm{m} + k_\mathrm{n} + \left(k_\mathrm{m} - k_\mathrm{n}\right) v_\mathrm{n}} \tag{2}$$

The overall composite's highest nanoparticle volume concentration was limited to 50%, corresponding to a 100% theoretical nanoparticle volume in the composite phase. Experimentally, only 40 vol% nanoparticle loading was achieved, corresponding to 20 vol% loading in the overall fiber. The calculation shows that layered fibers are 34% higher in thermal conductivity than uniform fibers at this concentration. Due to the challenges in experimentally measuring the thermal conductivity of anisotropic fibers, a transient plane source (TPS) method was used to estimate the thermal conductivity of rectangular bulk composites with different BN loadings,[75] followed by finite element analysis (FEA) to validate the relationship between thermal response and layer numbers computationally.

The TPS method uses a thin metal film, sandwiched between two identical composite samples, to generate Joule heat, and records the transient temperature response to estimate the thermal conductivity.[75] According to the measurement, the thermal conductivity increases monotonically and nonlinearly with BN volume concentrations from 0%, 5%, 10%, 15%, 20%, 30%, to 40% (Figure S16b, Supporting Information). The thermal conductivities between uniform (i.e., along with the channel directions, red in **Figure 5**a) and layered composites (i.e., from the Parallel–Maxwell–Eucken model as plotted blue in Figure 5a) show a more efficient heat dissipation for layered structures. For example, the thermal conductivities of the uniform BN/PVA and layered samples at a 20% BN loading are 0.94 and 1.26 W m^{-1} K^{-1}, respectively; a 34% increase for the layered structures. Similarly, to achieve a conductivity of 0.94 W m^{-1} K^{-1}, 20% BN is required for a uniform composite, while only 15% BN is required for a layered structure (Figure 5a). The thermal conductivity of a two-phase system depends not only on nanoparticle loading but also on the microstructure. After sintering the fibers at 800 °C, Figure 5b shows a clear image of the bare BN layers, consistent with the micro-CT images (Figure 3h,i); the preferentially aligned BN channels act as high ways for phonons to transport with a reduced scattering across boundaries.[38,39] On the other hand, homogeneously dispersed BN nanoparticles can be pictured as randomly distributed networks intercepted with local junctions, posing thermal dissipation and structure densification challenges.[76] Furthermore, the nonlinear relationship between the BN concentration and thermal conductivity predicts that such microstructure would be exponentially more effective as BN content increases.

FEA was used for layered composites to better understand the thermal profiles influenced by layer numbers. The experimentally measured thermal conductivity values of bulk PVA (0.38 W m^{-1} K^{-1}) and 40 vol% BN/PVA (2.15 W m^{-1} K^{-1}) were used for the alternating composite layer simulations. For comparison purposes, the bulk conductivity of 20 vol% BN/PVA was selected as the uniform composite. Under equal heating power (i.e., thermal field applied to the bottom fiber surfaces) and convection occurring on all other three edges, a higher thermal conductivity would result in a lower-temperature difference across the conduction path; in other words, a higher surface temperature in this FEA simulation correlates to higher thermal conductivity.[77] Figure 5c shows the simulation results as thermal contour maps, and Figure 5d shows the profiled top-surface temperature along with the x-coordinate. As the layer number increases, additional interfaces would replace the previous PVA–PVA interconnections with new BN–PVA interconnections, hence, increasing the interfacial conductivities (Figure S17, Supporting Information). In addition, the decreased layer thicknesses also result in a more uniform top surface temperature profile across alternating layers (e.g., 64L20% vs 4L20%, Figure 5d). The average fiber body temperatures of 5, 10, 15, and 20 vol% layered BN/PVA fibers are compared with the uniformly structured fibers, as summarized in Figure 5e. Layered structures show an apparent temperature increase at all BN concentrations, especially at higher BN vol%. Interestingly, the temperature increase eventually smoothed out with increased layer numbers. One possible explanation is that the new interfaces not only create BN–PVA interconnections from PVA–PVA interconnections but also destroy BN–BN interactions to form BN–PVA networking, causing a decrease in the thermal conductivity of the replaced BN/PVA layers (Figure S17, Supporting Information).

For application demonstration purposes, pure PVA and 32L20% fibers were handwoven into fabrics (5 cm by 5 cm in size) (Figure 5f) and placed on a Peltier plate as a heat source to test their time–temperature responses in an ambient environment. All fibers maintained a stable structure as their major axes were in contact with the heat source, aligning the BN heat pathways with the conducting direction (inset in Figure 5b). The high aspect ratio of the fiber ensures such a geometry after weaving without any additional precautions (Figure S18, Supporting Information). After the temperature stabilization, a series of infrared images were taken from 0 to 50 °C at a temperature step of 10 °C min^{-1} (Figure 5g). The 32L20%

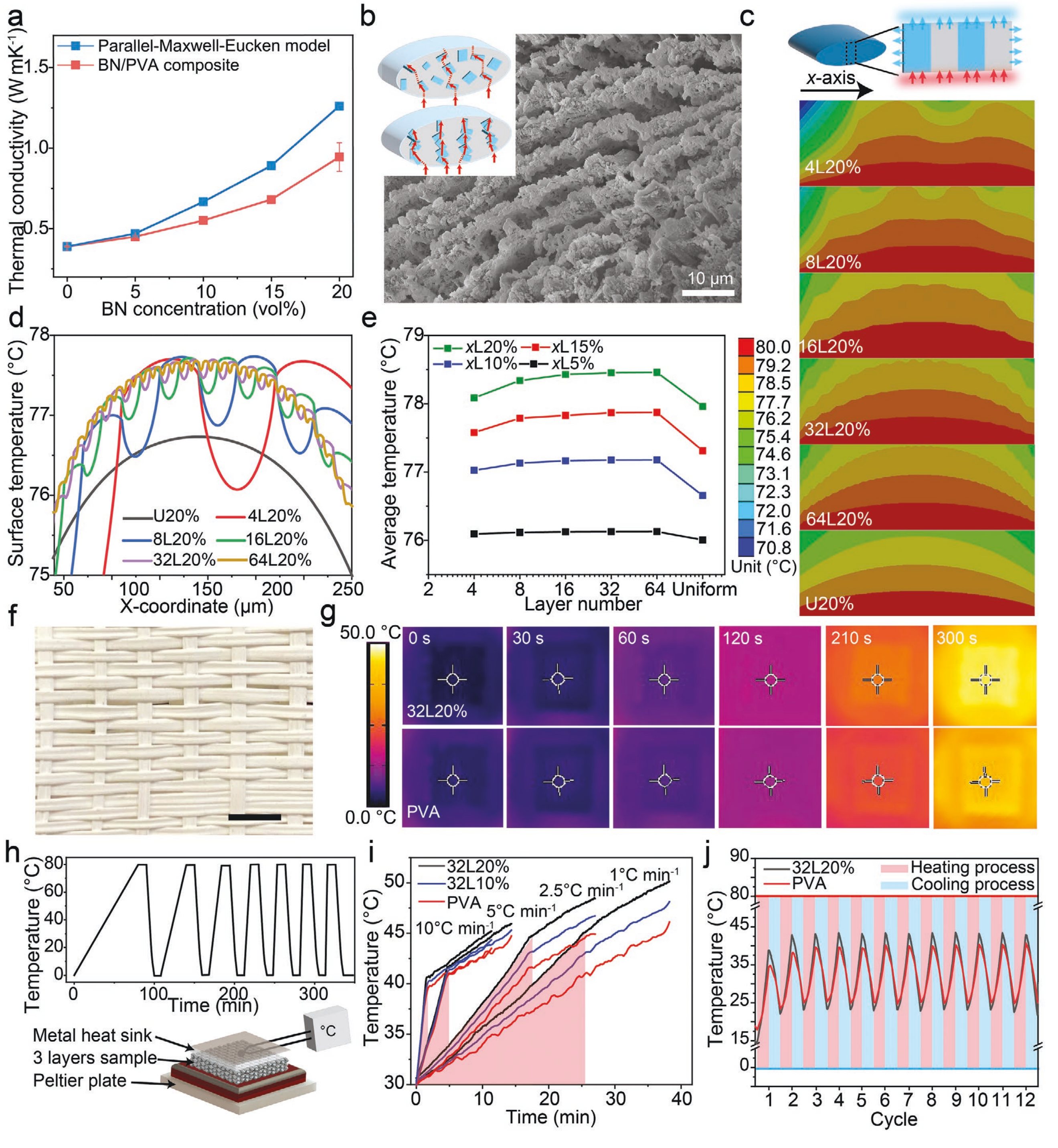

Figure 5. Thermal property–structure relationships and thermal demonstrations of wearable textiles composed of PVA or multilayered composite fibers. a) Theoretical thermal conductivity calculation of layered structure and experimental measurement of uniform structured BN/PVA composite fibers with SDs. b) Schematic illustration of the proposed thermal conductive pathways for uniform (the top inset) and layered (the bottom inset and the SEM image) fibers. c) Simulation result of 20 vol% BN/PVA fibers with different layer thicknesses. d) Top surface temperature profiles and e) averaged overall fiber temperatures. f) Handwoven 32L20% fiber fabric (scale bar = 2 mm) showed the thermal response differences between g) 32L20% fabrics (top) and pure PVA fabrics (bottom). h) An experimental setup (bottom schematic) with programmable heating rates (top figure) for measuring i) static and j) dynamic thermal responsiveness of the 32L20% and PVA fabrics.

fiber surface shows a lower starting temperature and a higher final temperature (Figure S19a, Supporting Information), and its absolute temperature difference between the heat source is lower than the pure PVA textile (Figure S19b, Supporting Information), indicating improved thermal conductivity. Moreover, the PVA, 32L10%, and 32L20% fabrics were tested under 1, 2.5, 5, and 10 °C min^{-1} heating rates to test the dynamic thermal conduction property. Three layers of each fabric were stacked together with a thermocouple attached on the topmost surface with silver paste to increase their temperature contrast (bottom schematic in Figure 5h). The heat source profile was programmable (top schematic in Figure 5h) with a 10 min steady-state period after each heating ramp. The thermal responses summarized in Figure 5i show that slower heating rates and higher BN concentration result in faster responses and vice versa. Furthermore, the responses of single-layer pure PVA and 32L20% fabrics under cyclic heating also show that the process is highly reversible between 0 and 80 °C (Figure 5j), indicating a large working window with mechanical robustness and material sustainability. Furthermore, the mechanical integrity of the multilayered fiber is essential for fabric performances as they undergo various deformations. Figure S20 (Supporting Information) shows the mechanical performances of 32L10% fibers under 280 cycles of 17% uniaxial strain compression with high-stress stability. Figure S20d_1,d_2 (Supporting Information) shows the SEM images of the fiber cross-sectional and surface morphologies. No obvious interfacial debonding was observed. Similarly, for 32L10% fiber under 140° torsion for 120 cycles, no obvious layer debonding was observed (Figure S20c,e_1,e_2, Supporting Information). We believe that the stable layer interface bonding is due to the single-step fabrication process, which enabled high PVA polymer chain entanglement between the PVA and BN/PVA layers. Such a behavior has also been previously reported by others for single-step fabricated coaxial multilayered structures.[24,78] The more dynamically stable interfaces from the polymer gel entanglement during the extrusion process showed improved interfacial delamination issues compared to the traditional layer-by-layer fabrication method.[24]

The layer multiplying technique is applicable in different material systems with varying manufacturing resolutions or versatile functionality. In addition to forming parallelly packed, thermally conductive pathways with BN nanoparticles, two other applications were briefly explored to show the general compatibility of our method with composite or hybrid materials. First, the alignment of channels can be controlled to construct not only parallel layers but also series layers (the left schematic in **Figure 6**a) with potential for thermal insulation applications as predicted by Figure 1a. A CFD simulation shows that by reversing the injection direction of feedstocks A and B across four multipliers, 16 alternating layers can be generated perpendicular to the minor axis direction (the right contour mapping in Figure 6a). As an example demonstration, material A was chosen as polyacrylonitrile (PAN), and material B was chosen as aluminum (Al)/PAN. After patterning the Al particles in a series sequence (Figure 6b_1), these metal powders were etched away to form pores aligned along the fiber major axis (Figure 6b_2; Figure S21, Supporting Information) with a layer thickness of 5–10 µm (Figure 6b_3). Similar to the Parallel/Maxwell–Eucken-coupled model, a Series–Maxwell–Eucken model was proposed based on Equation (3)

$$k_\mathrm{s} = \frac{1}{(1-\nu_2)/k_\mathrm{m} + \nu_2/k_2} \tag{3}$$

where ν_2 is the volume fractions of pores/polymer phase, k_m is the thermal conductivity of the polymer matrix, and k_2 is the thermal conductivity of the pores/polymer phase based on Equation (2).[37] With varied porosity that introduced the insulation space, Figure 6b_4 shows the thermal conductivities of fibers with pore-patterning (Series–Maxwell–Eucken model) and uniform pore distributions (Maxwell–Eucken model), implying greatly improved insulation efficiency via forming a higher porosity or concentrated pores within layers.

Apart from forming multilayered composites based on a single type of nanoparticle, the bi-nanoparticle laminate structure can also be feasible with the layer multiplication strategy, such as in cellulose nanocrystal (CNC)/cellulose nanofiber (CNF) stack films for structural coloration,[79] BN/graphene as dielectric nanocomposite,[80] or carbon nanotube (CNT)/BN for electromagnetic shielding application.[81] For a brief demonstration, BN and graphene nanoplatelets (GNPs) were mixed with PVA polymers as a binder to form eight alternating layers (Figure 6c_1), with each layer thickness of 20 µm (Figure 6c_2). Higher GNPs' concentrations increase the electrical conductivity after reaching the percolation threshold (5 wt%) along the fiber axial direction (Figure 6c_3). On the other hand, the electrically insulative BN nanoparticles prevent electron transport across the fiber (Figure 6c_3), resulting in over seven orders of magnitude difference in electrical conductivity between the along-fiber and perpendicular-to-fiber directions. Furthermore, previous research suggests that instead of forming a homogeneous mixer, a bilayer structure of graphene and BN results in enhanced thermal conductivity due to the higher interfacial thermal conductance between the homogeneous nanoparticle interfaces, such as BN/BN or graphene/graphene, than that of the BN/graphene interface, based on molecular dynamics simulations.[80,82]

3. Conclusion

This research reports the first-time use of a new fiber spinning technique for the simultaneous nanoparticle assembly to enhance structural patterning or functional properties in nanocomposites. Leveraging rapidly prototyped components in an in-house designed layer multiplying technique, we can selectively distribute and preferentially align different nanoparticles (e.g., BN, Al, and BN/GNPs) within thin-diameter, continuous fibers. Well-controlled material choices and flow behaviors would lead to layered structures, directed by CFD simulations and observed in experiments. First, composite layers can be designed with enhanced resistance to crack propagations (e.g., the PVA–BN/PVA layers). These nanocomposites also show programmable and directional heat dissipation capabilities by simply controlling the layer number and thickness (i.e., 2–65 µm). Second, the alternating layers' composition (e.g., different polymer/nanoparticle combinations) and structure (e.g., horizontally packed or vertically laminated) can be tailored depending on specific applications. For example, porous channels are selectively created via etching metal powders within specific layers, and ceramic hybrids are readily prepared as anisotropic conductors. At last, this manufacturing technique establishes a new mechanism in textile engineering that can be easily transferred and combined with other fabrication methods, such as knitting/weaving, coating/extrusion, direct

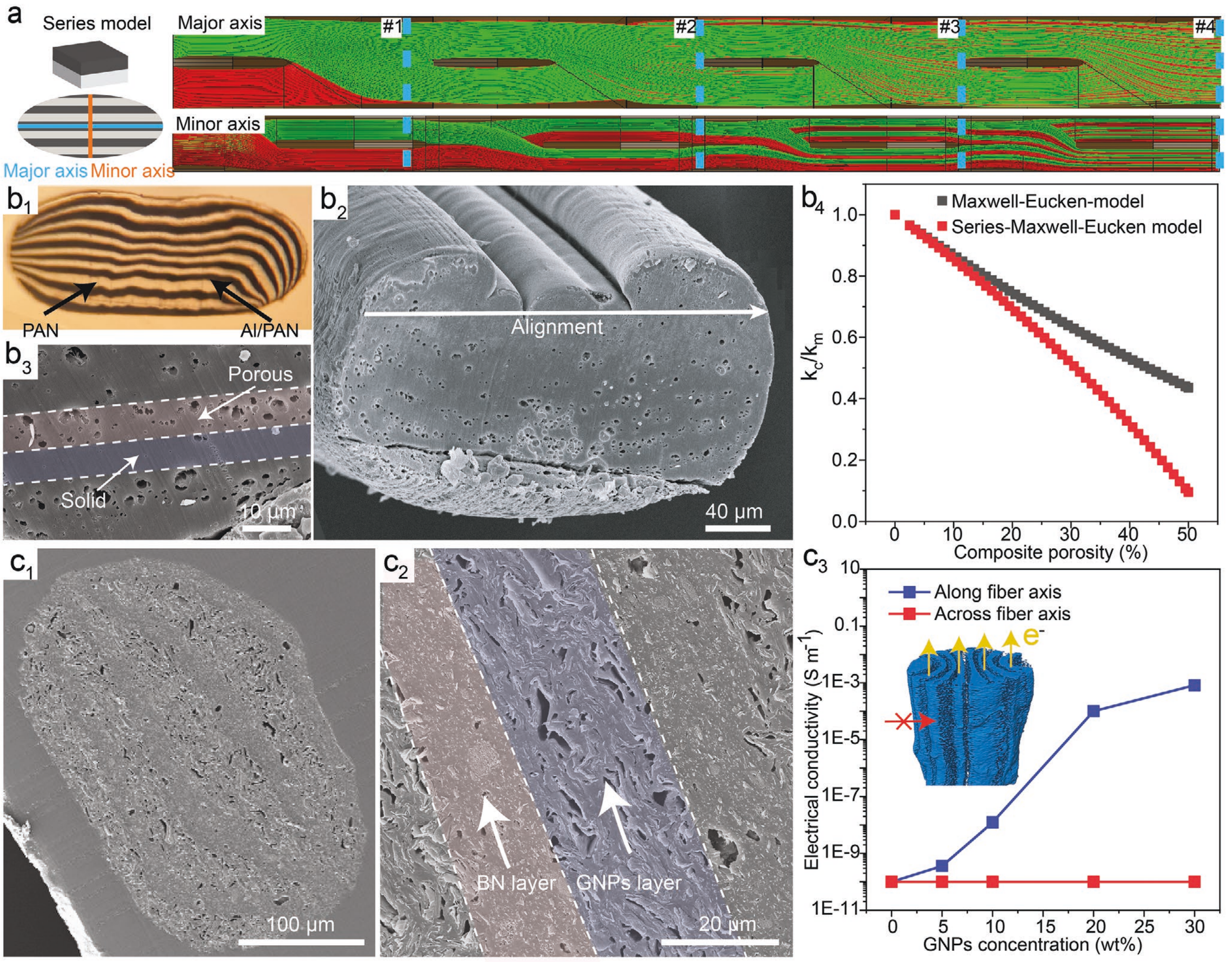

Figure 6. General applications of fiber layering technique in two other polymer/particle systems with thermal and electrical demonstrations. a) A CFD simulation of layer formability in the Series model predicts the layer formations. b_1) An optical image of the layered Al/PAN fiber, b_2) SEM imaging of the porous PAN fiber where the pores created by etching Al metals are aligned along the major axis direction. b_3) A zoomed-in SEM image of the pore-aligned layer and solid layer regions. b_4) Predicted thermal conductivity values based on the Series–Maxwell–Eucken model.[37] c_1,c_2) SEM images of alternating layers in BN/GNPs composite fibers. c_3) Measured anisotropic electrical conductivity of the thermally conductive fiber along and across the fiber axial direction.

ink writing, or fused deposition modeling, for scalable devices or systems, as demonstrated in our thermal-regulating fabrics.

4. Experimental Section

Materials: PVA (28-98) pellets were obtained from Kuraray, Japan, with a molecular weight of ≈145 000 g mol^{-1} and 98–99% degree of hydrolysis. PAN powder (230 000 g mol^{-1} and mean particle size 50 µm with the copolymer content of 99.5% acrylonitrile (AN)/0.5% methyl acrylate (MA)) was purchased from Goodfellow Corporation, USA. Hexagonal BN nanoparticles (99.5%) were purchased from Skyspring Nanomaterials Inc., USA. Aluminum particles (99%, 15 µm particle size), GNPs (xGnP M-5, 5 µm particle size, 120 m^2 g^{-1} surface area), DMSO (ACS reagent 99.9%), dimethylformamide (DMF) (ACS reagents, 99.8%), methanol (ACS reagent, 99.8%), and hydrochloric acid (ACS reagents, 37%) were purchased from Sigma–Aldrich, USA.

Layered Composites from BN/PVA Fiber Spinning: The multilayered spinneret was 3D-printed using Concept Laser M2 Cusing (i.e., the 3D printer from GE Additive, USA) with metallic powders of Inconel 718. For PVA spinning dope, desired weight concentrations of PVA powder (e.g., *x* wt%) were used to dissolve in DMSO solution at 100 °C with mechanical stirring until the solution became transparent. For BN/PVA spinning dope, 10 wt% of the desired PVA powder was first dissolved in DMSO, then mixed with desired BN nanoparticles for 30 min. The mixture was then sonicated in a sonication bath for 1 h. Next, the remaining PVA powder was added to this solution and mechanically stirred for 3 h at 100 °C. Next, pure PVA and BN/PVA spinning dopes were deaerated under vacuum for 1 h at 80 °C. Subsequently, the bubble-free spinning dopes were transferred into two separate stainless-steel syringes and then extruded at 1.5 mL min^{-1} speed through the 3D-printed spinneret into a methanol coagulation bath at room temperature with an air gap distance of 1 cm. After 24 h, these solidified fibers were first drawn at room temperature, followed by drying for 12 h in a vacuum at 50 °C. Finally, these dried fibers were drawn at 100 and 180 °C, respectively.

Porous PAN Fibers from Al/PAN Fiber Spinning: For the pure PAN layer, 15 wt% of PAN powder was added to DMF and was mechanically stirred at 80 °C for 3 h. For the hollow layers, 20 vol% of Al powder (i.e., with respect to PAN, 20 vol% Al/PAN) was added to 12 wt% PAN/DMF solutions (i.e., with respect to DMF weight, 12 wt% PAN dissolved in DMF), followed by 3 h of mechanical stirring at 80 °C. Then, both of these spinning dopes were deaerated under vacuum at 80 °C for 1 h before being injected via the in-house developed spinneret (same conditions as BN/PVA fiber spinning, i.e., at a rate of 1.5 mL min^{-1} into a methanol coagulation bath with an air gap distance of 1 cm at room temperature). The collected fibers were drawn immediately in water at 80 °C before forming gelled fibers in methanol and dried in a vacuum oven at 50 °C. At last, these dried fibers were placed into a 5 м HCl solution for 36 h to etch away the Al particles and generate porous PAN fibers.

Layered Multimaterial Hybrids from BN/GNPs Fiber Spinning: Desired weight percentages of GNPs and BNs were separately mixed with 1 g of PVA in DMSO, followed by 1 h of bath sonication. The remaining PVA powder was added and was mechanically stirred for 3 h at 100 °C. The solutions were deaerated in a vacuum oven for 1 h at 80 °C. Both solutions were injected into the spinneret inlet at 1.5 mL min^{-1} and through a methanol coagulation bath. The collected fiber was kept immersed in a methanol bath for 24 h, followed by drying at room temperature.

Characterizations: Rheological behaviors and uniaxial tensile tests were conducted using Discovery HR-2 (TA Instruments). For viscosity tests, a 40 mm, 2° Peltier plate was used with a truncation gap of 100 µm. For tensile tests, ten samples of each fiber type were tested with a gauge length of 2 cm and a gauge speed of 150 µm s^{-1}. SEM images were taken using Auriga FIB-SEM, Zeiss, GE. All samples were coated with 15 nm of Au/Pd to increase conductivity. 800 nm thick samples of the BN/GNPs' fiber were obtained from a microtome (Leica RM2235, GE) for SEM analysis. TGA was conducted in air at a heating rate of 10 °C min^{-1} (TGA 550, TA Instruments). DSC was conducted (DSC 250, TA Instruments) in N_2 with a scan rate of 10 °C min^{-1}. X-ray tomography was conducted using Xradia Versa 620 (ZEISS) with the dual-energy scanning method to enhance the contrast between layers having similar densities. Accelerating voltages of 40 and 150 kV were used. Voxel resolutions of 4.6 and 6.3 µm were obtained for the 8L10% and 16L10% fibers, respectively. Segmentation and rendering were done using the Dual Scan Contrast Visualizer (DSCoVer) (ZEISS) and Avizo 9.0 (FEI, Thermo Fisher Scientific), respectively. Thermal images were taken via an infrared camera E8-XT (Flir) with 320 × 240 pixel resolution.

Statistical Analysis: The SD for mechanical tests was based on ten samples for each fiber type. The SD for TPS measurements were based on five samples. The SD for layer thickness was based on three samples where each contains 4 to 64 layers.

Supporting Information

Supporting Information is available from the Wiley Online Library or from the author.

Acknowledgements

W.X. and R.F. contributed equally to this work. This work was funded by the Global Sports Institute (GSI) at Arizona State University and the U.S. National Science Foundation (NSF, EAGER 1902172).

Conflict of Interest

The authors declare no conflict of interest.

Data Availability Statement

The data that support the findings of this study are available from the corresponding author upon reasonable request.

Keywords

anisotropic, energy efficiency, multilayers, passive thermoregulators, polymer nanoparticle composites

Received: April 26, 2022
Revised: May 31, 2022

[1] J. Yang, W. Yang, W. Chen, X. Tao, *Prog. Polym. Sci.* **2020**, *109*, 101289.
[2] M. F. H. Wolff, V. Salikov, S. Antonyuk, S. Heinrich, G. A. Schneider, *Compos. Sci. Technol.* **2014**, *90*, 154.
[3] L. Zhang, X. Liu, A. Deb, G. Feng, *ACS Sustainable Chem. Eng.* **2019**, *7*, 19910.
[4] Y. Zhao, B. Zhang, B. Yao, Y. Qiu, Z. Peng, Y. Zhang, Y. Alsaid, I. Frenkel, K. Youssef, Q. Pei, X. He, *Matter* **2020**, *3*, 1196.
[5] L. Yin, K. N. Kim, J. Lv, F. Tehrani, M. Lin, Z. Lin, J. M. Moon, J. Ma, J. Yu, S. Xu, J. Wang, *Nat. Commun.* **2021**, *12*, 1542.
[6] Y. Cheng, Y. Ma, L. Li, M. Zhu, Y. Yue, W. Liu, L. Wang, S. Jia, C. Li, T. Qi, J. Wang, Y. Gao, *ACS Nano* **2020**, *14*, 2145.
[7] S. Z. Guo, K. Qiu, F. Meng, S. H. Park, M. C. McAlpine, *Adv. Mater.* **2017**, *29*, 1701218.
[8] Y. Chen, Z. Deng, R. Ouyang, R. Zheng, Z. Jiang, H. Bai, H. Xue, *Nano Energy* **2021**, *84*, 105866.
[9] Z. Wang, J. Ren, R. Liu, X. Sun, D. Huang, W. Xu, J. Jiang, K. Ma, Y. Liu, *Composites, Part A* **2020**, *136*, 105957.
[10] Y. Zhu, W. Xu, D. Ravichandran, S. Jambhulkar, K. Song, *J. Mater. Chem. A* **2021**, *9*, 8514.
[11] Y. Liu, X. Zhang, Y. Xia, H. Yang, *Adv. Mater.* **2010**, *22*, 2454.
[12] Y. Yang, X. Li, M. Chu, H. Sun, J. Jin, K. Yu, Q. Wang, Q. Zhou, Y. Chen, *Sci. Adv.* **2019**, *5*, eaau9490.
[13] S. Jambhulkar, W. Xu, D. Ravichandran, J. Prakash, A. Nadar, M. Kannan, K. Song, *Nano Lett.* **2020**, *20*, 3199.
[14] S. Jambhulkar, S. Liu, P. Vala, W. Xu, D. Ravichandran, Y. Zhu, K. Bi, Q. Nian, X. Chen, K. Song, *ACS Nano* **2021**, *15*, 12057.
[15] J. Chen, X. Liu, Y. Tian, W. Zhu, C. Yan, Y. Shi, L. B. Kong, H. J. Qi, K. Zhou, *Adv. Mater.* **2022**, *34*, 2102877.
[16] K. M. Pawelec, H. A. van Boxtel, S. G. J. M. Kluijtmans, *Mater. Sci. Eng., C* **2017**, *76*, 628.
[17] X. Wang, H. Zhai, B. Qie, Q. Cheng, A. Li, J. Borovilas, B. Xu, C. Shi, T. Jin, X. Liao, Y. Li, X. He, S. Du, Y. Fu, M. Dontigny, K. Zaghib, Y. Yang, *Nano Energy* **2019**, *60*, 205.
[18] L. Wang, X. Fu, J. He, X. Shi, T. Chen, P. Chen, B. Wang, H. Peng, *Adv. Mater.* **2020**, *32*, 1901971.
[19] X. Liang, H. Li, J. Dou, Q. Wang, W. He, C. Wang, D. Li, J. M. Lin, Y. Zhang, *Adv. Mater.* **2020**, *32*, 2000165.
[20] N. Wen, Z. Fan, S. Yang, Y. Zhao, C. Li, T. Cong, H. Huang, J. Zhang, X. Guan, L. Pan, *Chem. Eng. J.* **2021**, *426*, 130816.
[21] W. Xu, D. Ravichandran, S. Jambhulkar, R. Franklin, Y. Zhu, K. Song, *Adv. Mater. Technol.* **2020**, *5*, 2000440.
[22] Y. H. Lee, J. S. Kim, J. Noh, I. Lee, H. J. Kim, S. Choi, J. Seo, S. Jeon, T. S. Kim, J. Y. Lee, J. W. Choi, *Nano Lett.* **2013**, *13*, 5753.
[23] X. Yang, J. Wang, H. Guo, L. Liu, W. Xu, G. Duan, *e-Polymers* **2020**, *20*, 682.
[24] J. Zhao, H. Lu, Y. Zhang, S. Yu, O. I. Malyi, X. Zhao, L. Wang, H. Wang, J. Peng, X. Li, Y. Zhang, S. Chen, H. Pan, G. Xing, C. Lu, Y. Tang, X. Chen, *Sci. Adv.* **2021**, *7*, eabd6978.
[25] Y. Fang, G. Chen, M. Bick, J. Chen, *Chem. Soc. Rev.* **2021**, *50*, 9357.
[26] P. Liu, Y. Li, Y. Xu, L. Bao, L. Wang, J. Pan, Z. Zhang, X. Sun, H. Peng, *Small* **2018**, *14*, 1702926.
[27] M. Stoppa, A. Chiolerio, *Sensors* **2014**, *14*, 11957.

[28] S. Hong, Y. Gu, J. K. Seo, J. Wang, P. Liu, Y. Shirley Meng, S. Xu, R. Chen, *Sci. Adv.* **2019**, *5*, eaaw0536.
[29] Z. Liu, D. Qi, G. Hu, H. Wang, Y. Jiang, G. Chen, Y. Luo, X. J. Loh, B. Liedberg, X. Chen, *Adv. Mater.* **2018**, *30*, 1704229.
[30] E. P. Gilshteyn, S. Lin, V. A. Kondrashov, D. S. Kopylova, A. P. Tsapenko, A. S. Anisimov, A. J. Hart, X. Zhao, A. G. Nasibulin, *ACS Appl. Mater. Interfaces* **2018**, *10*, 28069.
[31] H. Sun, X. You, Y. Jiang, G. Guan, X. Fang, J. Deng, P. Chen, Y. Luo, H. Peng, *Angew. Chem., Int. Ed.* **2014**, *53*, 9526.
[32] J. Chen, H. Guo, X. Pu, X. Wang, Y. Xi, C. Hu, *Nano Energy* **2018**, *50*, 536.
[33] Z. Cong, W. Guo, Z. Guo, Y. Chen, M. Liu, T. Hou, X. Pu, W. Hu, Z. L. Wang, *ACS Nano* **2020**, *14*, 5590.
[34] J. Deng, Y. Zhang, Y. Zhao, P. Chen, X. Cheng, H. Peng, *Angew. Chem., Int. Ed.* **2015**, *54*, 15419.
[35] S. Rizal, F. G. Olaiya, N. I. Saharudin, C. K. Abdullah, N. G. Olaiya, M. K. Mohamad Haafiz, E. B. Yahya, F. A. Sabaruddin, Ikramullah, H. P. S. Abdul Khalil, *Polymers* **2021**, *13*, 325.
[36] C. Wang, T. Yokota, T. Someya, *Chem. Rev.* **2021**, *121*, 2109.
[37] L. Gong, Y. Wang, X. Cheng, R. Zhang, H. Zhang, *Int. J. Heat Mass Transfer* **2013**, *67*, 253.
[38] H. Chen, V. V. Ginzburg, J. Yang, Y. Yang, W. Liu, Y. Huang, L. Du, B. Chen, *Prog. Polym. Sci.* **2016**, *59*, 41.
[39] C. Huang, X. Qian, R. Yang, *Mater. Sci. Eng., R* **2018**, *132*, 1.
[40] J. Wang, J. K. Carson, M. F. North, D. J. Cleland, *Int. J. Heat Mass Transfer* **2008**, *51*, 2389.
[41] L. Gong, Y. Wang, X. Cheng, R. Zhang, H. Zhang, *Int. J. Heat Mass Transfer* **2014**, *68*, 295.
[42] Y. Cui, H. Gong, Y. Wang, D. Li, H. Bai, *Adv. Mater.* **2018**, *30*, 1706807.
[43] B. Grena, J. B. Alayrac, E. Levy, A. M. Stolyarov, J. D. Joannopoulos, Y. Fink, *Nat. Commun.* **2017**, *8*, 364.
[44] T. Gao, Z. Yang, C. Chen, Y. Li, K. Fu, J. Dai, E. M. Hitz, H. Xie, B. Liu, J. Song, B. Yang, L. Hu, *ACS Nano* **2017**, *11*, 11513.
[45] X. Yu, Y. Li, X. Wang, Y. Si, J. Yu, B. Ding, *ACS Appl. Mater. Interfaces* **2020**, *12*, 32078.
[46] D. Ravichandran, W. Xu, R. Franklin, N. Kanth, S. Jambhulkar, S. Shukla, K. Song, *Molecules* **2019**, *24*, 4142.
[47] Y. Gao, G. Yu, T. Shu, Y. Chen, W. Yang, Y. Liu, J. Long, W. Xiong, F. Xuan, *Adv. Mater. Technol.* **2019**, *4*, 1900504.
[48] X. Y. Du, Q. Li, G. Wu, S. Chen, *Adv. Mater.* **2019**, *31*, 1903733.
[49] P. V. Gulgunje, B. A. Newcomb, K. Gupta, H. G. Chae, T. K. Tsotsis, S. Kumar, *Carbon* **2015**, *95*, 710.
[50] M. Zhou, D. Hu, Y. Shao, J. Ma, J. Gong, *Mater. Sci. Forum* **2018**, *944*, 543.
[51] T. Ding, K. H. Chan, Y. Zhou, X. Q. Wang, Y. Cheng, T. Li, G. W. Ho, *Nat. Commun.* **2020**, *11*, 6006.
[52] J. Chen, H. Wen, G. Zhang, F. Lei, Q. Feng, Y. Liu, X. Cao, H. Dong, *ACS Appl. Mater. Interfaces* **2020**, *12*, 7565.
[53] W. Xu, S. Jambhulkar, R. Verma, R. Franklin, D. Ravichandran, K. Song, *Nanoscale Adv.* **2019**, *1*, 2510.
[54] W. Xu, D. Ravichandran, S. Jambhulkar, Y. Zhu, K. Song, *Adv. Funct. Mater.* **2021**, *31*, 2009311.
[55] R. Y. F. Liu, Y. Jin, A. Hiltner, E. Baer, *Macromol. Rapid Commun.* **2003**, *24*, 943.
[56] M. Ponting, A. Hiltner, E. Baer, *Macromol. Symp.* **2010**, *294*, 19.
[57] X. Li, G. B. Mckenna, G. Miquelard-garnier, A. Guinault, C. Sollogoub, G. Regnier, A. Rozanski, *Polymer* **2014**, *55*, 248.
[58] C. Chávez-Madero, M. D. De León-Derby, M. Samandari, C. F. Ceballos-González, E. J. Bolívar-Monsalve, C. Mendoza-Buenrostro, S. Holmberg, N. A. Garza-Flores, M. A. Almajhadi, I. González-Gamboa, J. F. Yee-De León, S. O. Martínez-Chapa, C. A. Rodríguez, H. K. Wickramasinghe, M. Madou, D. Dean, A. Khademhosseini, Y. S. Zhang, M. M. Alvarez, G. Trujillo-De Santiago, *Biofabrication* **2020**, *12*, 035023.
[59] J. Liu, W. Li, Y. Guo, H. Zhang, Z. Zhang, *Composites, Part A* **2019**, *120*, 140.
[60] D. Ravichandran, W. Xu, M. Kakarla, S. Jambulkar, Y. Zhu, K. Song, *Addit. Manuf.* **2021**, *47*, 102322.
[61] V. Kumar, V. Shirke, K. D. P. Nigam, *Chem. Eng. J.* **2008**, *139*, 284.
[62] M. Lu, J. Liao, P. V. Gulgunje, H. Chang, P. J. Arias-Monje, J. Ramachandran, V. Breedveld, S. Kumar, *Polymer* **2021**, *215*, 123369.
[63] K. Chatterjee, T. K. Ghosh, *Adv. Mater.* **2020**, *32*, 1902086.
[64] A. Etaati, S. Pather, Z. Fang, H. Wang, *Composites, Part B* **2014**, *62*, 19.
[65] Y. Rao, *Particuology* **2010**, *8*, 549.
[66] B. Oktay, N. Kayaman-Apohan, S. Erdem-Kuruca, *IOP Conf. Ser.: Mater. Sci. Eng.* **2014**, *64*, 012011.
[67] D. Papkov, N. Delpouve, L. Delbreilh, S. Araujo, T. Stockdale, S. Mamedov, K. Maleckis, Y. Zou, M. N. Andalib, E. Dargent, V. P. Dravid, M. V. Holt, C. Pellerin, Y. A. Dzenis, *ACS Nano* **2019**, *13*, 4893.
[68] K. Song, Y. Zhang, J. Meng, M. L. Minus, *J. Appl. Polym. Sci.* **2013**, *127*, 2977.
[69] R. Jan, P. May, A. P. Bell, A. Habib, U. Khan, J. N. Coleman, *Nanoscale* **2014**, *6*, 4889.
[70] V. Guerra, C. Wan, T. McNally, *Prog. Mater. Sci.* **2019**, *100*, 170.
[71] P. M. Ajayan, J. Suhr, N. Koratkar, *J. Mater. Sci.* **2006**, *41*, 7824.
[72] G. R. Liu, *Compos. Struct.* **1997**, *40*, 313.
[73] G. Szebényi, B. Magyar, T. Czigany, *Adv. Eng. Mater.* **2021**, *23*, 2000822.
[74] M. Fan, J. Domblesky, K. Jin, L. Qin, S. Cui, X. Guo, N. Kim, J. Tao, *Mater. Des.* **2016**, *99*, 535.
[75] R. Dai, G. Chandrasekaran, J. Chen, C. Jackson, Y. Liu, Q. Nian, B. Kwon, *Int. J. Therm. Sci.* **2021**, *169*, 107045.
[76] J. Hu, Y. Huang, X. Zeng, Q. Li, L. Ren, R. Sun, J. Bin Xu, C. P. Wong, *Compos. Sci. Technol.* **2018**, *160*, 127.
[77] P. Tervola, *Int. J. Heat Mass Transfer* **1989**, *32*, 1425.
[78] S. Tagliaferri, A. Panagiotopoulos, C. Mattevi, *Mater. Adv.* **2021**, *2*, 540.
[79] X. Zhang, R. Xiong, S. Kang, Y. Yang, V. V. Tsukruk, *ACS Nano* **2020**, *14*, 14675.
[80] F. Guo, X. Shen, J. Zhou, D. Liu, Q. Zheng, J. Yang, B. Jia, A. K. T. Lau, J. K. Kim, *Adv. Funct. Mater.* **2020**, *30*, 1910826.
[81] C. Lu, L. Yuan, Q. Guan, G. Liang, A. Gu, *J. Phys. Chem. C* **2018**, *122*, 5238.
[82] Y. C. Soong, C. W. Chiu, *J. Colloid Interface Sci.* **2021**, *599*, 611.